Journal of Computational Science and Technology

Vol. 7, No. 3, 2013

Characterization of Void Coalescence in Alpha-Iron in the Presence of Hydrogen*

Agung PREMONO**,*** and Hiroshi KANAYAMA****

** Department of Mechanical Engineering, Graduate School of Engineering, Kyushu University
744, Motooka, Nishi-ku, Fukuoka 819-0395, Japan
***Department of Mechanical Engineering, Faculty of Engineering, State University of Jakarta
Rawamangun Muka No.1, Jakarta, 13220, Indonesia
**** Department of Mechanical Engineering, Faculty of Engineering, Kyushu University
744, Motooka, Nishi-ku, Fukuoka 819-0395, Japan
E-mail : kanayama@mech.kyushu-u.ac.jp

Abstract

Characteristics of void coalescence process due to hydrogen load effects in the multiple void array are simulated using the finite element method. The goals of this paper are to characterize the effects of hydrogen on the void coalescence process within the multiple void array, and to determine the void array and void volume fraction configuration in which hydrogen has the strongest effect on the occurrence of void coalescence. We use the couple analyses between the large deformation elastic-plastic analysis in the presence of hydrogen for structural analysis and hydrogen diffusion analysis using the hydrogen enhanced localized plasticity (HELP) theory. These coupled analyses are applied to the five different models with the different void volume fraction and void array. The numerical results show that both hydrogen and the void characteristics – void array and void volume fraction – affect metallic material failure. The internal necking void coalescence occurs in the square void array while the void sheet mode of coalescence occurs in the diagonal void array. Hydrogen has the strongest effect on the occurrence of void coalescence when the void volume fraction is large and the void array is square, induces a pronounced localized plastic deformation at the ligament between voids, and is present in high concentrations in regions with high values of the equivalent plastic strain.

Key words: Void Coalescence, Void Volume Fraction, Void Array, Hydrogen Embrittlement, Coupled Analysis, Plastic Deformation

1. Introduction

Ductile fracture is a fracture which is characterized by plastic deformation in the vicinity of advancing crack. This plastic deformation can be recognized in the macro-scale by necking phenomena while in the micro-scale by void coalescence. Therefore, void coalescence is the critical stage of ductile fracture.

Void coalescence is reversed for the part of the void enlargement evolution after the transition to the mode of plasticity and an initiation process of the micro-crack deformation. Modes of void coalescence are (1) the internal necking mode of coalescence; (2) the void sheet mode of coalescence; and (3) the necklace coalescence[(1)]. Detail explanation of each mode can be seen in Appendix.

Many factors, such as initial void porosity, void volume fraction and void array, influence void coalescence. To evaluate these factors, many researchers studied the void

*Received 1 Apr., 2013 (No. 13-0156)
[DOI: 10.1299/jcst.7.395]

model using a cell model containing a single spherical void[2-7]. An assumption of these studies is that the void is in the same initial radius in a square array. Therefore, the void can be simplified to a single spherical void in one cell. A disadvantage of this method is that the interaction between voids can not be observed directly. To solve this, the void coalescence simulation using multiple voids is developed.

Some researchers have developed void coalescence using the multiple void model. Melander[8] investigated the fracture path on a random two-dimensional plane strain model under tension. Ohno and Hutchinson[9] developed a model to study the effect of void cluster on plastic flow localization. Dubensky and Koss[10] experimentally modeled the dependence of ductile, micro-void fracture, on the size and distribution of voids or pores. Magnusen et al.[11] developed a model to simulate the low temperature ductile fracture of metals which contained arrays of holes or voids. Bandstra et al.[12-14] experimentally and computationally modeled the void coalescence process using a void-sheet mechanism. Magnusen et al. [15] found that the void arrays, diameter of void, and distance between voids all affected ductile fracture. Hosokawa et al.[16] observed by X-ray tomography the effect of stress triaxiality on void growth and coalescence. However, most of them developed and simulated the void coalescence model of different geometric factors using structural boundary conditions only.

Other factors, such as temperature, pressure, and the presence of some gases e.g. hydrogen also influence void coalescence. Hydrogen-material interaction has been a particular concerning due to the effects of hydrogen on the metallic materials such as reducing yield stress, decreasing fracture toughness, and accelerating crack growth. This undesirable interaction – one of hydrogen embrittlement phenomena – is still a mysterious phenomenon. To date, some researchers investigated the effects of hydrogen on void coalescence[17-19]. All of these investigations simulated using a cell model containing a spherical void.

In the present research, the effects of hydrogen on void coalescence process are characterized in the multiple void array. With this characterization, we show a clearer understanding of the effects of hydrogen on the void coalescence process within the multiple void array in the several void volume fractions, and predict the void array and void volume fraction in which hydrogen has the greatest effect on the occurrence of void coalescence. Structure of this paper is as follows: Section 2 and Section 3 review the hydrogen transport equation and the constitutive law for the large elastoplastic analysis in the presence, respectively. Section 4 presents the coupled analysis specification between structural analysis and hydrogen diffusion analysis in materials, and material properties. Section 5 describes the modeling and boundary conditions and Section 6 discusses the numerical results. Section 7 concludes this work.

2. The hydrogen transport equation

In this section, we explain the hydrogen diffusion equation which refers to Krom et al.[20]. This formulation is rewritten in order to describe how structural load affects the hydrogen concentration. The hydrogen diffusion equation with the suitable initial and boundary conditions in this research is defined by:

$$\frac{C_L + C_T\left(1-\theta_T\right)}{C_L}\frac{\partial C_L}{\partial t} - \nabla\cdot\left(D_L\nabla C_L\right) + \nabla\cdot\left(\frac{C_L D_L \bar{V}_H}{RT}\nabla\sigma_h\right) + \theta_T\frac{dN_T}{d\varepsilon_p}\frac{\partial\varepsilon_p}{\partial t} = 0, \qquad (1)$$

where C_L and C_T are the main unknown hydrogen concentration in the lattice and the auxiliary hydrogen concentration in trap sites, respectively, $\theta_{L(T)}$ is the occupancy of lattice (or trap) sites which is defined by ratio of occupied sites to the total available, $N_{L(T)}$ is the

number of lattice (or trap) sites per unit volume, $\overline{V}_H$ is the partial molar volume of hydrogen, R is the gas constant [J/(mol K)], and T is the absolute temperature (K). $D_L = M_L RT$ is the concentration independent lattice diffusivity, where M_L is the mobility of hydrogen in lattice sites. We only need the value of D_L in our computation, and in this case D_L is the lattice diffusion constant ($1.27\times10^{-8}\ m^2/s$) [21]. All of constant parameter values in Eq. (1) refers to Sofronis et al.[21] which can be seen in Table 1. The reason because the material in this research is alpha iron. σ_h is the hydrostatic stress which is defined by $\sigma_h = \frac{\sum \sigma_{ii}}{3}$, where σ_{ii} is the stress components, and ε_p is the equivalent plastic strain. These two quantities are obtained from the structural analysis which is explained in the coming section. The final equation of the hydrogen transport equation may refer to Kanayama et al.[22]. The properties of material and hydrogen diffusion parameters are summarized in Table 1.

Table 1. Material properties and hydrogen diffusion parameters[21]

Young's modulus, E	207 Gpa
Poisson ration, v	0.3
Initial yield stress, σ_Y	250 MPa
The work hardening exponent, n	0.2
Gas constant, R	8.3144 J / mol K
Partial molar volume of hydrogen, $\overline{V_{\mathrm{H}}}$	2×10^{-6} m^3/mol
Lattice sites per unit volume N_{L}	5.1×10^{29} m^{-3}
Trap binding energy, Δ E $_{\mathrm{T}}$	-6×10^3 J / mol

3. The constitutive equation for large deformation elastoplastic analysis in the presence of hydrogen

To simulate the hydrogen effects on the structural analysis, we consider a non-linear finite element analysis for the large deformation elastoplastic analysis. The non-linearity mainly comes from the nonlinear relationship between stresses and strains. In the non-linear analysis, we use the equilibrium of the body considered in the current configuration. With this, we adopt the updated Lagrangian (UL) formulation to solve the equilibrium equation. The constitutive formulation for the large deformation elastoplastic analysis in the presence of hydrogen in this study refers to Liu et al.[23] which is defined by:

$$
\begin{aligned}
d^{t+\Delta t}\sigma = \Bigg\{ & C^* - \frac{\left(C^* : {}^{t+\Delta t}\sigma'\right)\otimes\left(C^* : {}^{t+\Delta t}\sigma'\right)}{{}^{t+\Delta t}\sigma' : \left(C^* : {}^{t+\Delta t}\sigma'\right) + \frac{4}{9}\gamma\, {}^{t+\Delta t}h\, {}^{t+\Delta t}\overline{\sigma}^2} \\
& + \frac{\left(C^* : {}^{t+\Delta t}\sigma'\right)\otimes\left(C^* : \delta\right)\left[{}^{t+\Delta t}\sigma' : \left(C^* : {}^{t+\Delta t}\sigma'\right)\right]{}^{t+\Delta t}\mu}{\left({}^{t+\Delta t}\sigma' : \left(C^* : {}^{t+\Delta t}\sigma'\right) + \frac{4}{9}\gamma\, {}^{t+\Delta t}h\, {}^{t+\Delta t}\overline{\sigma}^2\right)\frac{2}{3}\, {}^{t+\Delta t}h\, {}^{t+\Delta t}\overline{\sigma}} \\
& - \frac{\left(C^* : {}^{t+\Delta t}\sigma'\right)\otimes\left(C^* : \delta\right){}^{t+\Delta t}\mu}{\frac{2}{3}\, {}^{t+\Delta t}h\, {}^{t+\Delta t}\overline{\sigma}} \Bigg\} : d\, {}^{t+\Delta t}e \\
= {} & C^{ep} : d\, {}^{t+\Delta t}e\ ,
\end{aligned}
\tag{2}
$$

where ${}^{t+\Delta t}\sigma$ and ${}^{t+\Delta t}e$ are stress and strain tensors corresponding to time $t+\Delta t$, σ' is the deviatoric part of the Cauchy stress tensor defined through $\sigma' = P:\sigma$. $P = I - J$ is the

deviatoric part of the fourth order identity tensor I whose Cartesian components are $I_{ijkl}=\left(\delta_{ik}\delta_{jl}+\delta_{jk}\delta_{il}\right)/2$. $J=\delta\otimes\delta/3$ is the hydrostatic part of the identity tensor, and δ is the second order identity tensor. $^{t+\Delta t}h=\frac{\partial^{t+\Delta t}\sigma_Y}{\partial^{t+\Delta t}\bar{e}^p}+\frac{\partial^{t+\Delta t}\sigma_Y}{\partial^{t+\Delta t}c}\frac{\partial^{t+\Delta t}c}{\partial^{t+\Delta t}\bar{e}^p}$ is the slope of the yield function ($\bar{\sigma}=\sigma_Y\left(\bar{e}^p,c\right)$) curve, $^{t+\Delta t}\mu=-\frac{\partial^{t+\Delta t}\sigma_Y}{\partial^{t+\Delta t}c}\frac{\partial^{t+\Delta t}c}{\partial^{t+\Delta t}\sigma_{kk}}$ is the pressure sensitivity of yield, and $\gamma=\left(1-2\,^{t+\Delta t}h\Delta\lambda/3\right)^{-1}$. $C^*=\left(\left(C^e\right)^{-1}+\Delta\lambda P\right)^{-1}$ with the superscript -1 denoting the tensor inverse. C^e is the fourth order tensor of the elastic modulus. $\bar{\sigma}$ is the von-Mises equivalent stress which is defined by

$$\bar{\sigma}^2=\frac{3}{2}\left(\sigma':\sigma'\right). \tag{3}$$

The differential formulation of a kinematic parameter $(\Delta\lambda)$ with respect to time $t+\Delta t$ is

$$d\left(\Delta\lambda\right)=\frac{^{t+\Delta t}\sigma':d^{t+\Delta t}\sigma+\frac{2}{3}\gamma^{t+\Delta t}\mu\;^{t+\Delta t}\bar{\sigma}\,d^{t+\Delta t}\sigma_{kk}}{\frac{4}{9}\gamma^{t+\Delta t}h\;^{t+\Delta t}\bar{\sigma}^2}. \tag{4}$$

The equivalent plastic strain at time $t+\Delta t$ $\left(^{t+\Delta t}\bar{e}^p\right)$ is decomposed as:

$$^{t+\Delta t}\bar{e}^p=\,^t\bar{e}^p+\Delta\bar{e}^p=\,^t\bar{e}^p+\frac{2}{3}\Delta\lambda^{t+\Delta t}\bar{\sigma}\,, \tag{5}$$

where $^t\bar{e}^p$ is the equivalent plastic strain at time *t*, $\Delta\bar{e}^p$ is the increment of the equivalent plastic strain. $\bar{e}^p$ is the equivalent plastic strain which is the same quantity with ε_p in Eq. (1).

According to the von-Mises yield criteria, where the yield criterion is the form of Eq (3) and $F_Y=\frac{1}{3}\left(\bar{\sigma}^2-\sigma_Y^2\right)$, the material yields if $F_Y=0$. Then, we have

$$\bar{\sigma}=\sigma_Y\left(\bar{e}^p,c\right), \tag{6}$$

where σ_Y is the yield stress. In this research, the yield stress refers to the local softening model of flow stress in the presence of hydrogen proposed by Sofronis et al.[21]. The main reason for the use of this consideration is that the material in this research is alpha iron. Even though a new model to describe hydrogen effects on materials by considering softening and hardening phenomena proposed by Miresmaeli et al.[24] has been presented, this model is suitable only for stainless steel. Miresmaeli et al.[24] report that hydrogen causes softening in pure iron. The local softening model by Sofronis et al. is defined by[21]:

$$\sigma_Y=\sigma_0(c)\left(1+\frac{\varepsilon_p}{\varepsilon_0}\right)^n\,, \tag{7}$$

where $c=\frac{C_L+C_T}{N_L}$ is the normalized total hydrogen concentration in traps and normal interstitial lattice sites (NILS), $\varepsilon_0=\sigma_0/E$ is the initial yield strain which corresponds to the initial yield stress in the absence of hydrogen, and n is the work hardening exponent. $\sigma_0(c)$ is the yield stress in the presence of hydrogen, as suggested by Kotake et al.[25] and is given in a linear form $\sigma_0(c)=(\xi c+1)\sigma_0$, where ξ is a coupled effect parameter to represent the behavior of yield stress due to hydrogen absorption.

C^{ep} in Eq. (2) is the fourth-order elastoplastic constitutive tensor with the backward Euler integration process accounting for the hydrogen-induced material softening, defined as the first part of Eq. (2).

4. Coupled analysis specification, modeling, and boundary conditions

We implement a full coupled analysis between hydrogen diffusion and large deformation elastoplastic analyses, as shown in a flowchart in Fig. 1. In the first step, we analyze the large deformation elastoplastic analysis by considering the initial hydrogen concentration. In this step, the initial hydrogen concentration in trap sites is assumed negligible. Due to this assumption, the initial hydrogen concentration in NILS is equal to the normalized total hydrogen concentration. This is indicated by the upper red arrow. The calculation can not be done if there is no hydrogen concentration input. From this analysis, we obtain the nodal values of displacement, hydrostatic stress, and equivalent plastic strain in the presence of hydrogen. These results are transferred to the diffusion analysis to calculate the new hydrogen concentration by considering the structural load. These processes are indicated by the lower red arrow. The new hydrogen concentration calculation can not be done if there are no structural analysis results as an input. At the end of each increment of diffusion analysis, the new hydrogen concentration is updated. This new hydrogen concentration is taken as the new input for hydrogen diffusion analysis as long as the process is not over. This value is transferred to the structural analysis to calculate the nodal values of displacement, hydrostatic stress, and equivalent plastic strain in the presence of hydrogen at the next step of analysis. We apply this flowchart throughout analyses for all models and explain details in the upcoming paragraphs.

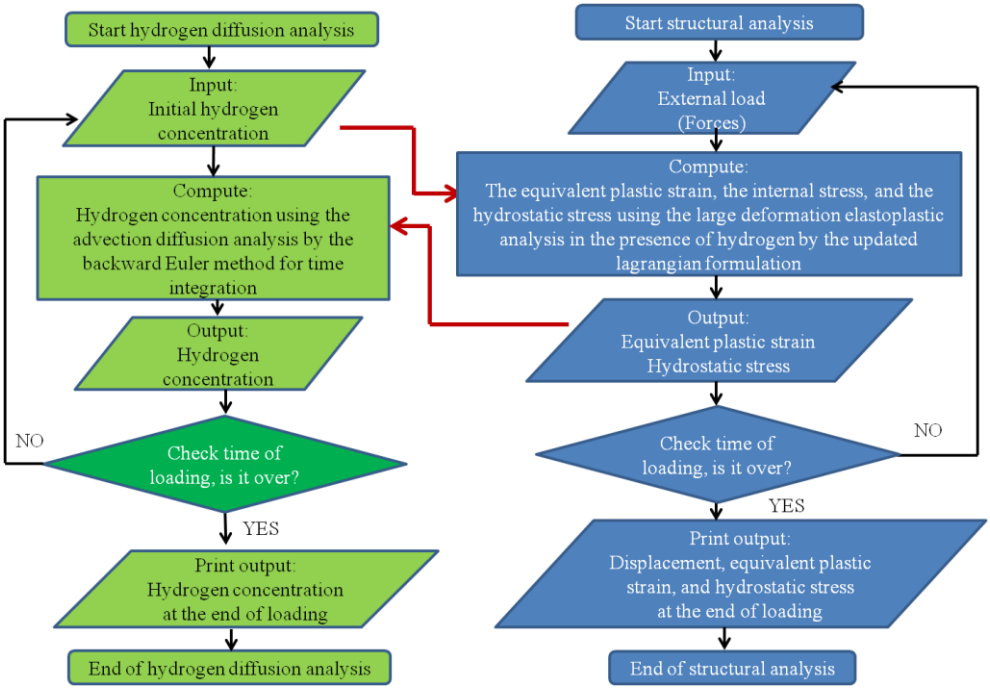

Fig. 1. A flow chart showing the coupled analysis specification

We simulate a tensile model containing voids with a notch. Basically, we construct two models with the different void array, square and diagonal, as shown in Fig. 2. However, to create difference void volume fraction in each void array, we create five models based on the void array and void volume fraction differences. Two of these models, A and B, have square void arrays with the same initial void volume fraction (f_0) = 0.14 and uniform initial radius (R_0) of 27 μm and 20 μm respectively. The third model, C, also has square void arrays with f_0 = 0.08 and uniform R_0 = 20 μm. The distance between voids for these three models in the *x*- and *y*-direction is the same, 80 μm. The last two models, D and E, have diagonal void arrays with uniform initial radius (R_0) 27

μm and 20 μm for $f_0 = 0.14$ and $f_0 = 0.08$, respectively. For models D and E, the same distance in the diagonal direction in the *x*- and *y*- axis is given, 113.137 μm. The length, width and notch radius for all models are 3.92×10^{-3} m , 6.4×10^{-4} m , and 20×10^{-6} m, respectively. All models are summarized in Table 2.

We apply the displacement controlled load to attain 12 % strain in 100 seconds with time step 0.5 second at one end of the model in the *y*-direction while the other end is constrained in the same direction. We constraint one node at the bottom center of the specimen in the *x*-direction (at the point A in Fig. 2). To simulate plane strain behavior, we implement a very thin 3D mesh with full constraints in the *z*-direction throughout the analysis. We set the constant hydrogen concentration C_b on the outer boundaries , denoted by the red lines, at C_{L0} where C_{L0} is set to 0 (hydrogen free) and 1 ppm. We assume that the void and notch faces are impermeable to hydrogen. We apply the initial hydrogen concentration uniformly throughout the domain Ω before straining and is equal to C_{L0}. We apply these boundary conditions to all models. We use the general-purpose finite element program MSC Marc[26] for the structural analyses with a user subroutine that incorporates a softening model using the 8-node hexahedral element. To analyze the hydrogen diffusion, we use our in-house hydrogen diffusion code using the 4-node tetrahedral element. These boundary conditions are shown in Fig. 2.

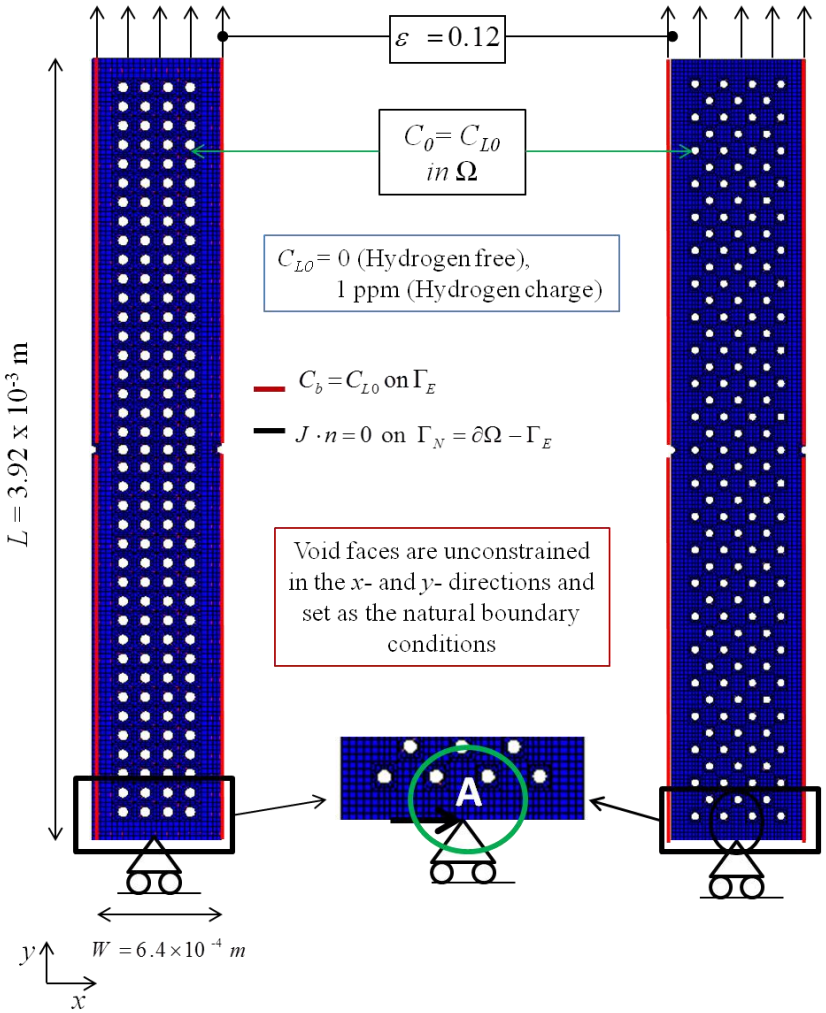

Fig. 2 Model and boundary conditions

Table 2 Summary of all models

	Void array	Initial void volume fraction (f_0)	Initial void radius (R_0)	Number of holes
Model A	Square	0.14	20 μm	288
Model B	Square	0.14	27 μm	156
Model C	Square	0.08	20 μm	156
Model D	Diagonal	0.14	27 μm	158
Model E	Diagonal	0.08	20 μm	158

5. Numerical Results

The first parameter to characterize the hydrogen effects on several void coalescence models is the stress-strain graph. Figure 3 shows the stress in the *y*-direction against the strain in the same direction for all models in the absence of hydrogen and in the presence of hydrogen with initial hydrogen concentrations. The stress-strain relationship is obtained by measuring these quantities at the center of the specimen (at the point O in Fig. 3) because we set the constant elongation data. For all analyses, the total axial strain (ε) is defined as $\varepsilon = \ln\left(1+\left(\Delta l/l_0\right)\right)$ where Δl is the incremental displacement in the *y*-direction and l_0 is the initial length. This figure shows that hydrogen reduces the stress in all models. This result is consistent with the experimental result [27].

Figure 3 shows that the stress in the model with a square void array with $f_0 = 0.14$ is larger than the model with $f_0 = 0.08$. The different phenomena occur in the model of the diagonal void array. The stress on the model with a diagonal void array and void volume fraction $f_0 = 0.14$ is smaller than the stress on the model with the void volume fraction $f_0 = 0.08$. However, the percentage decrease of the stress due to the hydrogen load are the same, in which the hydrogen has the greatest effect on the stress decrease which occurs in the large void volume fraction as can be seen in Table 3. These phenomena show that the stress and the void coalescence are affected by the void volume fraction. The onset of void coalescence is also observed at a certain level of strain when the initial void volume fraction (f_0) is equal to 0.14 in the presence of hydrogen, while it is not observed at $f_0 = 0.08$. These results show that hydrogen has the greatest effect on the occurrence of void coalescence when the void volume fraction is large. This conclusion shows good agreement with the previous study[19].

Figure 3 also shows that the stresses on the square void array are larger than the stresses on the diagonal void array in the absence and presence of hydrogen. To determine the effects of void arrays on void coalescence in the presence of hydrogen, decreasing the stress in the *y*-direction is observed, as shown in Table 3. From this table, it can be seen that the greatest decreasing of the stress in the *y*-direction occur in the square void array (in Model B). From these results, it can be concluded that hydrogen has the strongest effect on the occurrence of void coalescence when the void array is square.

To determine in which model the hydrogen has the greatest effect to decrease the stress, we show the highest stress value at the point O in Fig 3. These values are summarized in Table 3. This percentage decrease in this table represent decreasing the stress in the presence of hydrogen which is defined by $(\%) = \dfrac{\text{values } \mathbf{A} - \text{values } \mathbf{B}}{\text{values } \mathbf{A}} \times 100\,\%$. From this table it can be concluded that hydrogen has the greatest effect to reduce the stress in Model B, which is about 9.90 % lower than the stress in the absence of hydrogen.

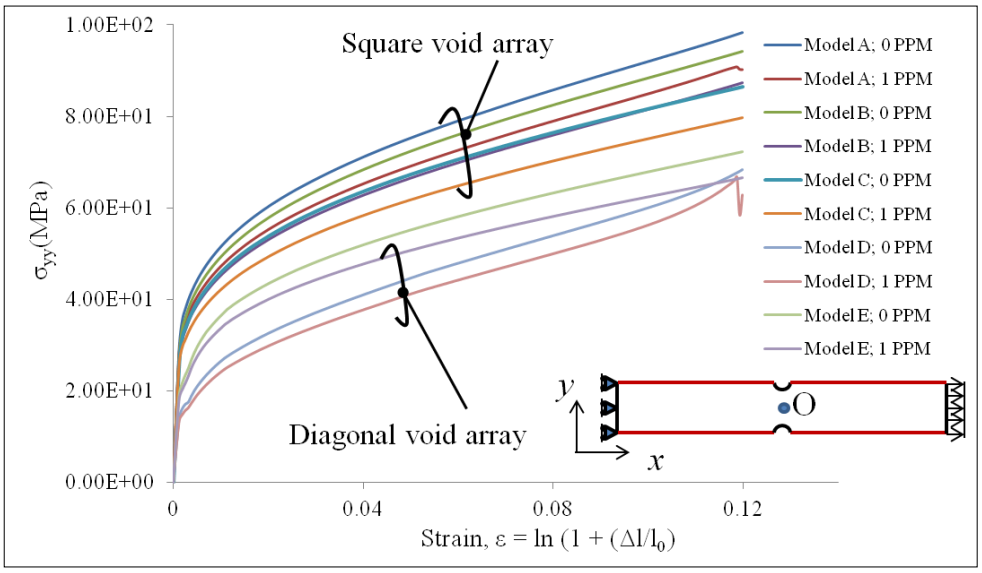

Fig. 3 Stress strain graph for all models

Table 3. The highest stress value measured at the center of the specimen (point O in Fig. 3) in the absence and presence of hydrogen

Model	Stress measured (σ_{yy}) (MPa)		The percentage decrease (%)
	In the absence of hydrogen (Values **A**)	In the presence of hydrogen (Values **B**)	
Model A	9.42e+02	8.73e+02	7.32
Model B	1.04e+03	9.40e+02	9.90
Model C	8.66e+02	7.98e+02	7.85
Model D	6.83e+02	6.29e+02	7.91
Model E	7.22e+02	6.65e+02	7.89

The second parameter to characterize the hydrogen effects on void coalescence on several models is the equivalent plastic strain. Contour plots of the equivalent plastic strain for Model A and Model D are shown in Figs. 4 and 5, respectively. We define that the contour plot of the equivalent plastic strain is a tendency for void coalescene which is in turn fracture path. From these figures we can see that void array and hydrogen affect the fracture. Figure 4 shows that the fracture path is perpendicular to the main loading direction in both cases, in the absence and presence of hydrogen. However, the fracture path in the presence of hydrogen is more visible than in the absence of hydrogen. The different fracture path occurs in the diagonal void array as shown in Fig. 5. In this figure, hydrogen induces a pronounced localized plastic deformation at the ligament between voids. It is at 45^0 to the main loading direction. In both square and diagonal void array cases, hydrogen induces plastic deformation at the ligament between voids. This result is consistent with the previous study[17]. The values of the equivalent plastic strain are much higher in the presence of hydrogen than that in the hydrogen free environment, which shows a tendency for the fracture path formation in the path of void coalescence. The maximum equivalent plastic strain appears close to the surface of the imperfection in all cases. However, the highest value of increasing the equivalent plastic strain value due to the hydrogen load occurs in Model A, which is about 36% greater than that in the absence of hydrogen. The equivalent plastic strain

values for all models are summarized in Table 4. The percentage increase in this table represent increasing the equivalent plastic strain value due to hydrogen load effects which is defined by $(\%)=\frac{\textbf{values D}-\textbf{values C}}{\textbf{values C}}\times 100\,\%$. From these results, we can conclude that hydrogen has the strongest effect on the occurrence of void coalescence when the void volume fraction is large and the void array is square. To validate these two conclusions, we refer to previous studies. The first conclusion is consistent with the previous study[19]. However, due to the limitation of the experimental data and the previous study, the second part of this conclusion is validate in the absence of hydrogen only. The conclusion in the second part show good agreement with the experimental study[1] where fracture mainly occurs in the square void array in the absence of hydrogen.

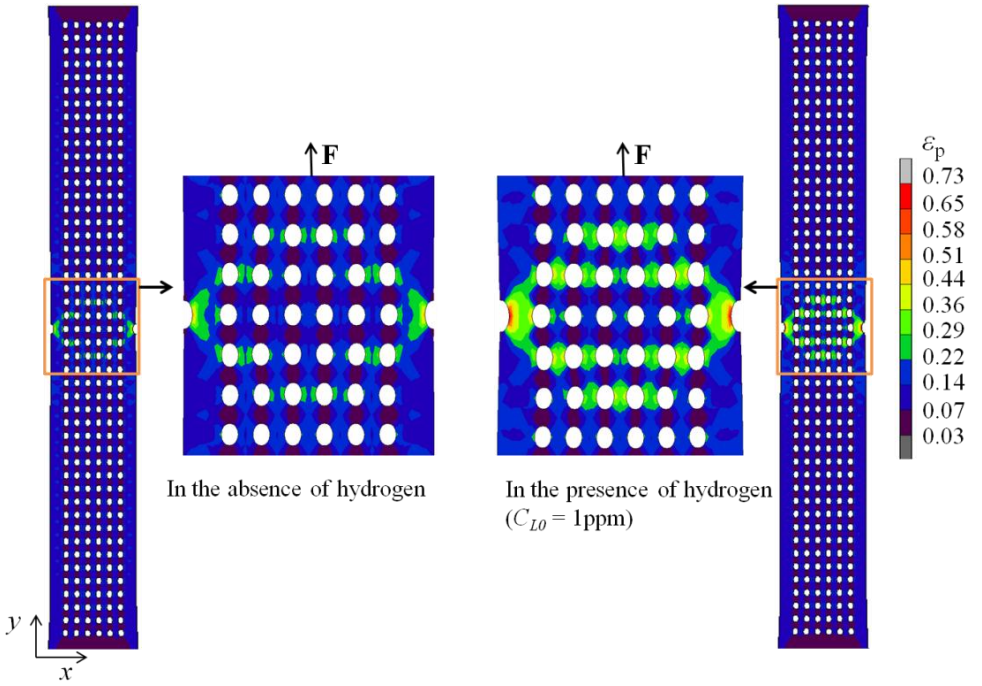

Fig. 4 The equivalent plastic strain contour plot on Model A in the absence and presence of hydrogen (square void array; $f_0 = 0.14$; and $R_0 = 27$ μm)

Table 4. The equivalent plastic strain values for different void array and initial void volume fraction (f_0) in the absence and presence of hydrogen

Model	Equivalent plastic strain value in the absence of hydrogen (Values **C**)	Equivalent plastic strain value in the presence of hydrogen (Values **D**)	Percentage increase (%) (%) = {([**D**-**C**]/**C**) x 100%}
Model A	0.5324	0.7259	36.34
Model B	0.4835	0.5198	7.51
Model C	0.4622	0.4822	4.33
Model D	0.8024	0.9746	21.46
Model E	0.514	0.623	21.20

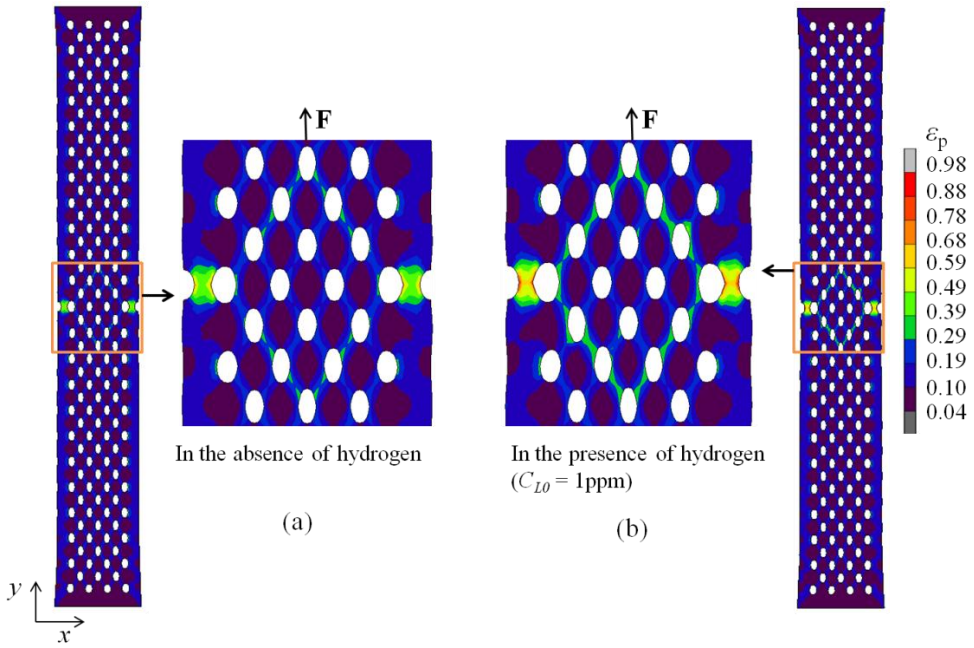

Fig. 5 The equivalent plastic strain contour plot on Model D in the absence and presence of hydrogen (Diagonal void array; $f_0 = 0.14$; and $R_0 = 27$ μm)

Figure 6 shows the contour of equivalent plastic strain for the different initial void volume fraction models (Model A and Model C). From this figure, we can see that the fracture path depends on the void volume fraction and distance between holes. When the diameter of the holes is different (and therefore the void volume fraction is also different), the contour of equivalent plastic strain is slightly different. Strain band is more obvious at $f_0 = 0.14$ than at $f_0 = 0.08$ for all models. Furthermore, the highest value of equivalent plastic strain occurs in Model D in which the initial void volume fraction $f_0 = 0.14$, while the lowest values of this quantitiy occurs in Model C in which $f_0 = 0.08$, as can be seen in the Table 4. In the case where hydrogen is present, similar results occur in all cases. However, in order to determine the effects of void volume fraction in the presence of hydrogen accurately, the increasing percentages of equivalent plastic strain are observed as shown in Table 4. This table shows that the largest percentage increase of the equivalent plastic strain occurs in Model A. The equivalent plastic strain values in Model B and Model D are larger than the equivalent plastic strain in Model C and Model E. These results show that hydrogen has the strongest effect on the occurrence of void coalescence when the initial void volume fraction is large as observed in the present result. This result is consistent with the previous study[19] .

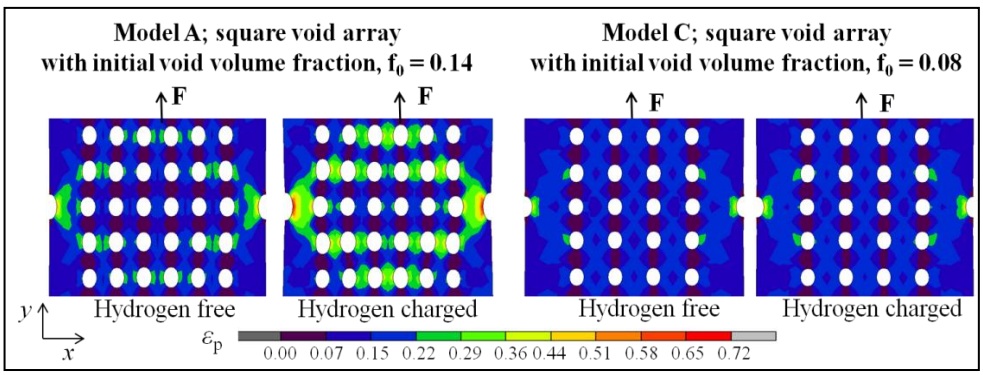

Fig. 6 Contour plot of equivalent plastic strain for Model A and Model C.

To maintain the total void volume fraction even with different initial hole diameters, models with different numbers of holes are constructed. The fracture path is observed to be perpendicular to the loading direction when the distance between holes is small, while the fracture path is observed to be at 45^0 to the loading direction when the distance between holes is large. These are shown in Fig. 7. From this figure, it can be concluded that the distance between holes and the hole diameter affect the fracture path even though the void volume fraction is the same.

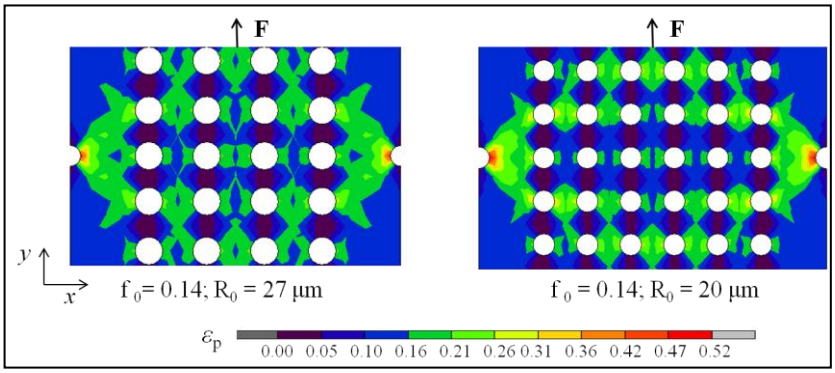

Fig. 7 The equivalent plastic strain contour for different initial diameters in the presence of hydrogen for: (a) Model B (R_0 = 27 μm; f_0 = 0.14), and (b) Model A (R_0 = 20 μm; f_0 = 0.14)

The dependence of the macroscopic fracture behavior on the different void array is shown in Fig. 8. In the case where the void diameter is same, the fracture path is similar between the diagonal void array and the square void array. The fracture path is observed to be at 45^0 to the loading direction. This means that the void sheet mode coalescence occurs in these models. In addition, the effect of hydrogen is more visible in the diagonal void. However, the fracture path is completely different when the number of holes is changed. The fracture path is observed to be perpendicular to the loading direction in Model A where the initial radius of holes (R_0) is 20 μm and number of holes is 288 holes as can be seen in Fig. 4. Therefore, the internal necking mode of coalescence can be obtained in this model. The previous study[1] mention that the most common mode of coalescence is the internal necking mode. Therefore, the same condition occurs in the present study. In this model, the highest hydrogen effects on void coalescence may occur.

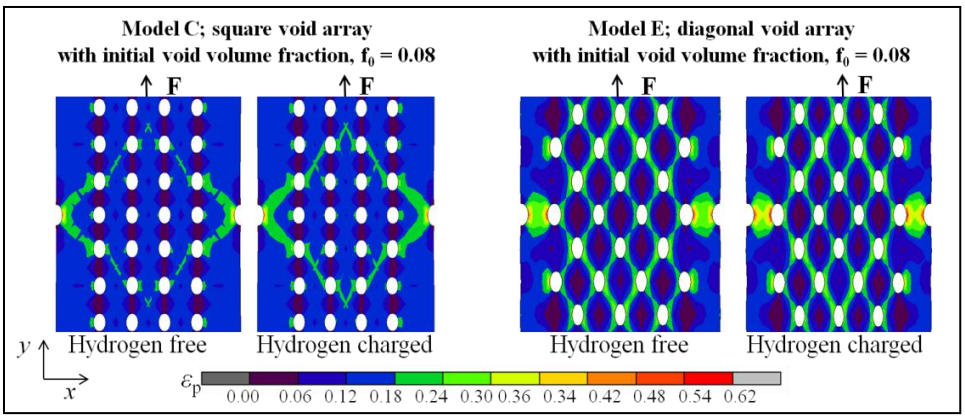

Fig. 8 Contour plots of the equivalent plastic strain in the absence and presence of hydrogen for Model C (square void array; f_0 = 0.08; and R_0 = 20 μm) and Model E (diagonal void array; f_0 = 0.08; and R_0 = 20 μm).

The third parameter to characterize the effect of hydrogen on the different void array and void coalescence is the void diameter growth. Figure 9 illustrates the diameter of the void shown in the figure in the *x*-direction, D_x, as a function of strain in the presence and absence of hydrogen for Model A. The red and purple curves show D_x of Hole 1 in the presence and absence of hydrogen, respectively, and the blue and green curves show D_x of Hole 2 in the presence and absence of hydrogen, respectively. In the case where hydrogen is absent, from the initiation of load up to a level of strain ($\varepsilon = 0.1$), the diameters of Hole 1 and Hole 2 decrease. However, after this level of strain, the diameters of these holes increase. In the case where hydrogen is charged, the diameter increases along with increasing of strain. This means that the effects of hydrogen on void growth and coalescence become stronger, and the length in the *x*-direction of the void in the presence of hydrogen increases significantly. It indicates that the void is elongated in the direction perpendicular to the tensile direction in the presence of hydrogen. Hydrogen promotes void growth perpendicular to loading direction; thus, macroscopic failure can take place more easily than in the hydrogen free case even though the macroscopic deformation is smaller than that in the hydrogen free case where void growth is parallel to the loading direction. This numerical result shows good agreement with the experimental results obtained by Murakami et al.[28]. This may be considered as a possible cause of hydrogen embrittlement.

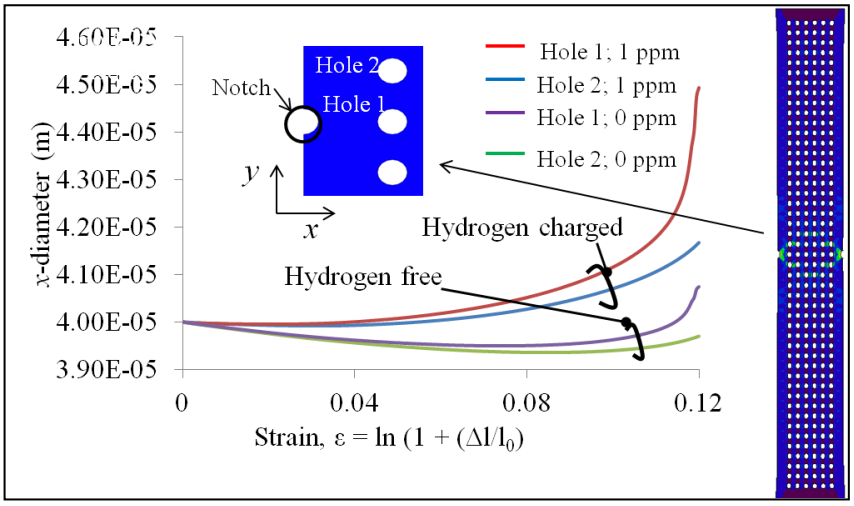

Fig. 9 Plots of the diameters in the *x*-direction versus strain with and without hydrogen for Model A; $f_0 = 0.14$, $R_0 = 20$ μm; square void array

6. Summary

The numerical results indicate that hydrogen induces a pronounced localized plastic deformation at the ligament between voids and accelerates void coalescence. These can be seen from the results that voids in the presence of hydrogen grow at a much faster rate than in hydrogen-free cases at larger plastic strain. Meanwhile, the void volume fraction is an important factor that affects the deformation mode. The fracture path is perpendicular to the loading direction at $f_0 = 0.14$, whereas the fracture path is 45^0 to the loading direction at $f_0 = 0.08$. The stress at $f_0 = 0.14$ is larger than at $f_0 = 0.08$ for square void array, whereas the stress at $f_0 = 0.08$ is larger than at $f_0 = 0.14$ for the diagonal void array. In addition, the void array affects the stress. In fact, the stress on the square void array is larger than the stress on the diagonal void array. Hydrogen has the strongest effect on the occurrence of void coalescence when the void volume fraction is large and the void array is square. High hydrogen concentrations are located in regions with high values of the equivalent plastic strain.

Acknowledgement

This work was supported by JSPS KAKENHI Grant Number 25840142.

Appendix

The internal necking void coalescence mode is macroscopically oriented at 90^0 (perpendicular) with respect to the main loading direction. The ligament between the two voids shrinks with a shape typical of a necking process. The voids evolve toward a diamond shape . This mode is illustrated in Fig. A.1.

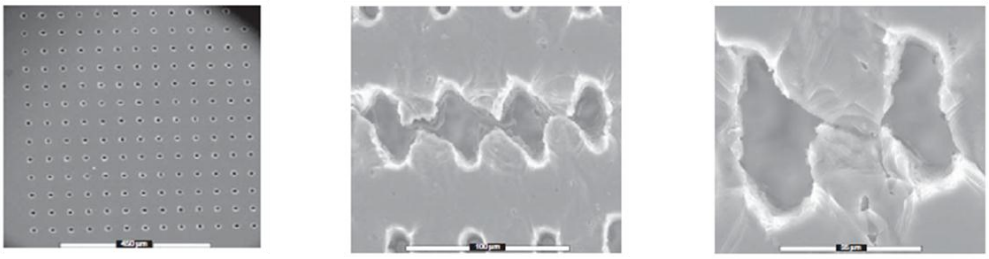

Fig. A.1. Internal necking void coalescence mode[1]

The void-sheet void coalescence mode consists of a shear localization between large primary voids observed when the initial voids are distributed along lines 45^0 from the main loading direction, as illustrated in Fig. A.2. This mode of coalescence is frequently observed in high-strength materials with low or moderate strain hardening capacity.

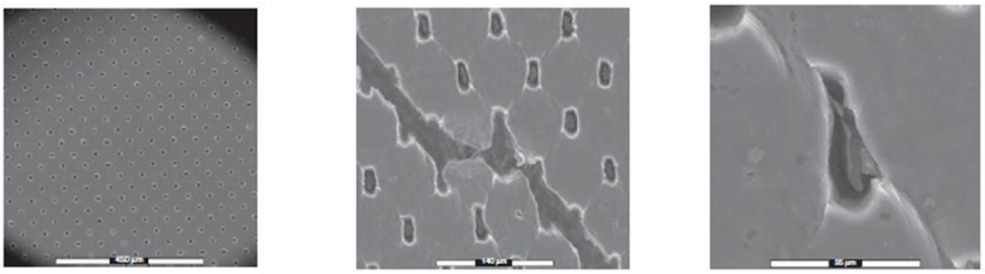

Fig. A.2. Void-sheet void coalescence mode [1]

The third mode of void coalescence, called ‘necklace coalescence’, is observed in between rows of voids gathered in elongated clusters. It consists of a localization process in a direction parallel to the main load, as shown in Fig. A.3.

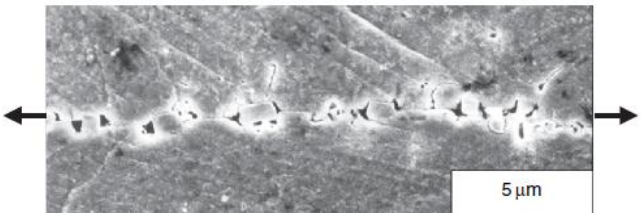

Fig. A.3. Necklace void coalescence mode[1]

References

(1) Pineau, A., Pardeon, T., Failure of metals, *Comprehensive structural integrity*, 2, Elsevier, (2007), pp. 684-797.
(2) Koplik, J., Needleman, A., Void growth and coalescence in a porous plastic solids, *Int. J. Solids Structures*, 24 (8) (1988), pp. 835 - 853.
(3) Pardeon, T., Hutchinson, J.W., An extended model for void growth and coalescence, *Journal of the Mechanics and Physics of Solids*, 48 (2000), pp. 2467 – 2512.
(4) Thomason, P.F., Three-dimensional models for the plastic limit-load at incipient failure of the intervoid matrix in ductile porous solids, *Acta Metallurgica* 33, (1985a) pp. 1079 – 1085.
(5) Thomason, P.F., A three-dimensional model for ductile fracture by the growth and coalescence of microvoids, *Acta Metallurgica* 33, (1985b), pp. 1087 – 1095.
(6) Benzerga, A.A., Micromechanics of coalescence in ductile fracture, *Journal of the Mechanics and Physics of Solids*, 50 (2002), pp. 1331 – 1362.
(7) Scheyvaerts, F., Pardeon, T., A new model for void coalescence by internal necking, *International Journal of Damage Mechanics*, 19, (2010), pp. 95 – 126.
(8) Melander, A., Computer simulation of ductile fracture in a random distribution of voids, *Materials Science and Engineering* 39, (1979), pp. 57 – 63.
(9) Ohno, N., Hutchinson, J.W., Plastic flow localization due to non-uniform void distribution, *J. Mech. Phys. Solids*, 32, 1, (1984), pp. 63 – 85.
(10) Dubensky, E.M., Koss, D.A., Void/pore distributions and ductile fracture, *Metallurgical Transactions* A, 18 A, (1987), pp. 1887 – 1895.
(11) Magnusen, P.E., Srolovitz, D.J., Koss, D.A., A simulation of void linking during ductile fracture microvoid fracture, *Acta Metall. Mater.* 38, 6, (1990), pp. 1013 – 1022.
(12) Bandstra, J.P., Goto, D.M., Koss, D.A., Ductile fracture as a result of void sheet instability: experiment and computational modeling, *Material Science and Engineering* A249, (1998), pp. 46 – 54.
(13) Bandstra, J.P., Koss, D.A., Modelling the ductile fracture process of void coalescence by void-sheet formation, *Material Science and Engineering* A319-321, (2001), pp.490 – 495.
(14) Bandstra, J.P., Koss, D.A., Geltmacher, A., Matic, P., Everett, R.K., Modeling void coalescence during ductile fracture of a steel, *Material Science and Engineering* A366, (2004), pp. 269 – 281.
(15) Magnusen, P.E., Dubensky, E.M., Koss, D.A., The effect of void arrays on void linking during ductile fracture, *Acta metall*, 36 (6), (1988), pp. 1503 – 1509.
(16) Hosokawa, A., Wilkinson D.A., Kang, J., Maire, E., Effect of triaxiality on void growth and coalescence in model materials investigated by X-ray tomography, *Acta Materialia* 60, (2012), pp. 2829 – 2839.
(17) Ahn, D.C., Sofronis, P., Dodds Jr., R.H., On hydrogen-induced plastic flow localization during void growth and coalescence, *International Journal of Hydrogen Energy*, 32 (2007), pp. 3734 – 3742.
(18) Ahn, D.C., Sofronis, P., and Dodds Jr., R.H., Modeling of hydrogen-assisted ductile crack propagation in metals and alloys, *Int J Fract* 145, (2007), pp. 135-157.
(19) Liang, Y., Ahn, D.C., Sofronis, P., Dodds Jr., R.H., Bammann, D., Effect of hydrogen trapping on void growth and coalescence in metals and alloys, *Mechanics of Materials* 40, (2008), pp. 115-132.
(20) Krom, A. H. M., Koers, R. W. J., Bakker, A., Hydrogen transport near a blunting crack tip, *Journal of the Mechanics and Physics of solids*, Vol. 47, (1999), pp. 971-992.
(21) Sofronis, P., Liang, Y., Aravas, N., Hydrogen induced shear localization of the plastic flow in metals and alloys, *European Journal of Mechanics - A/Solids*, Vol. 20, (2001),

pp. 857-872.

(22) Kanayama, H., Shingoh, T., Ndong-mefane, S., Ogino, M., Shioya, R., Kawai, H., Numerical Analysis of Hydrogen diffusion problems using the finite element method, *Theoretical and Applied Mechanics Japan*, Vol.56, (2008), pp. 389-400.

(23) Liu, L., Miresmaeili, R., Ogino, M., Kanayama, H., Finite element implementation of an elastoplastic constitutive equation in the presence of hydrogen, *Journal of Computational Science and Technology*, Vol. 5, No.1, (2011), pp. 62-76.

(24) Miresmaeili, R., Liu, L., Kanayama, H., A possible explanation for the contradictory results of hydrogen effects on macroscopic deformation, *International Journal of Pressure Vessels and Piping*, Vol. 99-100, (2012), pp. 34-43.

(25) Kotake, H., Matsumoto, R., Taketomi, S., Miyazaki, N., Transient hydrogen diffusion analyses coupled with crack-tip plasticity under cyclic loading, *International Journal of Pressure Vessels and Piping*, Vol. 85, (2008), pp. 540–549.

(26) MSC Marc 2005 r3 volume A: theory and user information, *MSC Software Corporation*, (2006).

(27) Matsuoka, S., Homma, N., Tanaka, H., Fukushima Y., and Murakami, Y., Effect of hydrogen on the tensile properties of 900-MPa-class JIS-SCM435 low-alloy-steel, *J. Japan Inst. Metals*, Vol. 70, No. 12, (2006), pp. 1002-1011, (In Japanese).

(28) Murakami, Y., Matsuoka, S., Effect of hydrogen on fatigue crack growth of metals, *Engineering Fracture Mechanics*, Vol. 77, 11, (2010), pp.1926-1940.